POLITECNICO
MILANO 1863

RE.PUBLIC@POLIMI
Research Publications at Politecnico di Milano

Post-Print

This is the accepted version of:

J.-S. Ardaens, G. Gaias
Flight Demonstration of Spaceborne Real-Time Angles-Only Navigation to a Noncooperative Target in Low Earth Orbit
Acta Astronautica, Vol. 153, 2018, p. 367-382
doi:10.1016/j.actaastro.2018.01.044

The final publication is available at https://doi.org/10.1016/j.actaastro.2018.01.044

Access to the published version may require subscription.

When citing this work, cite the original published paper.

© 2018. This manuscript version is made available under the CC-BY-NC-ND 4.0 license
http://creativecommons.org/licenses/by-nc-nd/4.0/

Permanent link to this version
http://hdl.handle.net/11311/1139191

Flight Demonstration of Spaceborne Real-Time Angles-Only Navigation to a Noncooperative Target in Low Earth Orbit

Jean-Sébastien Ardaens[1], Gabriella Gaias

DLR, German Aerospace Center, 82234 Wessling, Germany

Abstract

The paper describes the onboard vision-based navigation software employed during the DLR's AVANTI experiment and presents its flight performance. The navigation task relies on a dedicated target detection module in charge of extracting the line-of-sight observations from the images taken by a monocular camera. The recognition of the target is based on the kinematic identification of its trajectory over a sequence of images. Subsequently, the resulting angles-only measurements are validated dynamically and processed by an Extended Kalman Filter to derive in real-time the relative state estimate. A computationally light implementation of the filter is achieved by the use of an analytical relative motion model. Two autonomous rendezvous to a noncooperative object have been performed in orbit, first from 13 km to 1 km separation, then from 3 km to 50 m. Despite the poor visibility conditions and the strong orbit perturbations encountered at low altitude, the filter was able to supply the onboard guidance and control algorithms with accurate and reliable relative state estimation, enabling thus a safe and smooth approach.

Keywords: noncooperative rendezvous, angles-only navigation, autonomy, formation-flying, flight demonstration

Email address: jean-sebastien.ardaens@dlr.de (Jean-Sébastien Ardaens)
[1]Corresponding author.

1. Introduction

In-orbit technological realizations always constitute a priceless mine of lessons learned and valuable experience, and the AVANTI (Autonomous Vision Approach Navigation and Target Identification) demonstration is no exception. This experiment was successfully conducted by the German Aerospace Center (DLR/GSOC) in autumn 2016 and could demonstrate spaceborne autonomous rendezvous to a noncooperative target using solely line-of-sight measurements [1].

The spaceborne algorithms, constituting the core of the experiment, have been embedded as passenger software on BIROS, a German Earth observation satellite launched in June 2016 as part of the FireBird constellation [2]. This choice was motivated by the fact that this spacecraft was carrying a third-party picosatellite (BEESAT-4 [3]) to be released in orbit using a dedicated ejection mechanism [4], which means that an appealing target was already available to support the experiment without the need of spending propellant to rendezvous with an existing object. In addition, BIROS could grant access to the key hardware devices required by the experiment: a camera and a propulsion system. No additional formation-flying sensors or actuators were used. As a consequence, the entire experiment has been designed to use one of the star cameras as unique sensor to track the target object.

AVANTI has been developed relying on the experience already collected in 2012 using the PRISMA formation flying testbed. At that time, the so-called ARGON (Advanced Rendezvous demonstration using GPS and Optical Navigation [5]) experiment had already tackled the problem of angles-only relative navigation by exercising a ground-in-the-loop approach to a noncooperative target using optical methods. Compared to this precursor experiment, AVANTI presents an increased level of complexity to cope with a more realistic scenario such as rendezvous to space debris or a noncooperative satellite to be serviced [1].

One of the major advances brought by AVANTI is summarized by the first

letter of the experiment name: Autonomy. For this purpose a real-time onboard navigation filter is needed to supply the guidance and control algorithms with accurate estimate of the state of the formation. As sketched out in the second section, the navigation filter employed by AVANTI processes the line-of-sight measurements to the target spacecraft, which are previously extracted by a dedicated target detection algorithm from the images collected onboard using one of the star cameras of the satellite. It has to be emphasized that the experiment has been conceived to deal with a truly uncooperative target, relying only on pictures to estimate precisely the state of the formation. As a matter of fact, the images collected in orbit were the only available observations since the GPS receiver embarked by BEESAT-4 [6] was unfortunately not yet operational during the time slot allocated to AVANTI.

AVANTI intends to increase the available expertise in the field of angles-only navigation. In the past years, this domain has attracted lots of attention and its possible use for autonomous orbital rendezvous has been recognized from early on [7, 8]. Among the related research topics, the problem of observability has garnered considerable effort [9, 10, 11, 12], specifically the quest to understand which maneuvers improve the observability most significantly and which relative trajectories provide the best relative navigation performance [13]. More recently, the problem of angles-only navigation even in the absence of maneuvers was also investigated [14].

The experimental nature of the AVANTI demonstration represents a major contribution to this research field. The aforementioned investigations are in fact rather theoretical. All the authors take for granted the availability of a set of bearing observations. In reality, the extraction of the measurements from the images is sometimes challenging, which justifies the need for advanced target recognition algorithms. Until now the in-orbit experience with angles-only navigation has been rather limited, making the emergence of any well-established reliable method for target detection difficult. Orbital Express [15] exercised autonomous rendezvous using passive imagery in 2007, but the lack of published technical details is an obstacle to assess what exactly has been achieved. The

activities done with the PRISMA technology demonstrator [16] represent a more valuable reference. Several angles-only experiments have been executed by the different partners of the mission. In particular, the former Swedish Space Corporation and the French space agency (CNES) both conducted autonomous rendezvous based on angles-only navigation [17, 18] using line-of-sight observations extracted in real-time by a dedicated software feature built into the far-range camera. Within the PRISMA mission, DLR's activities were instead designed to work directly with the pictures output by the camera and culminated with the above-mentioned ARGON. However, this was not an autonomous experiment.

The built-in target detection software [19] of the vision-based sensor used for PRISMA constitutes to the authors' knowledge one of the rare existing autonomous target detection systems. Being implemented directly in the camera system, the algorithm is able to run at high frequency (2 Hz) and detects non-stellar objects based on their expected inertial angular velocity. The sensor keeps track internally of all the detected objects and delivers only the best candidate based on the luminosity and the number of sequential detections. In spite of this, during the PRISMA operations some false detections were still reported. Reference 17 mentions for example that a bright star was erroneously flagged as non-stellar object during several orbits while Reference 18 indicates an average of 4 wrong measurements observed during the three 16h-long rendezvous exercised by CNES. In addition, this strategy appears more difficult to implement considering the low image rate used during AVANTI (one image every 30 seconds). During the ARGON experiment, a target detection algorithm based on linking bright connected sets of pixels over sequences of images had been used [20]. However, this algorithm was also subject to some misdetections [5]. For AVANTI, a novel algorithm based on the kinematic detection of target trajectories has been developed. The underlying idea is that the target object obeys the law of space dynamics so that its apparent trajectories can be recognized as a curve, adding additional robustness to the detection algorithm. In addition, the algorithm exploits, in a second step, its connection to the relative navigation task to further filter out the possible outliers.

The second major contribution of AVANTI lies in the experience gained under a very challenging experimental context, which makes the authors believe that the worst possible relative navigation conditions have been reached during the experiment. Extensive analyses had been conducted during the development of the onboard filter using an advanced simulation environment. However, the experimental conditions were even worse than the simulated worst case. The paper addresses specifically the lessons learnt which have been collected during the experimental timeline. Overall, the weak observability of line-of-sight navigation has been a recurrent issue throughout the whole experiment. This problem is well-known, and its solution is to execute calibrated maneuvers to change the formation configuration over time [11]. As explained in the first section, three additional major obstacles have been constantly contributing to degrade the observability, creating challenging conditions for the navigation filter: a poor visibility, an unknown time-varying differential drag, and large maneuver execution errors (up to 6 mm/s).

Despite all these difficulties, the paper shows that AVANTI's filter design was perfectly suited for the needs of the experiment. Two approaches have been performed autonomously: from 13 km to 1 km (19-23 November 2016) and from 3 km to 50 m (25-28 November, 2016) [1]. Initialized from the ground with a guess of the relative state derived from Two-Line Elements (accurate to a few hundred meters), the filter was able to support the onboard controller with a navigation solution accurate at the meter level in the lateral direction and to about 10% of the intersatellite separation in the boresight direction. In the absence of other sensors to independently evaluate the state of the formation, the filter performance has been assessed using precise relative orbit determination generated on ground using the same set of data [21].

It has to be noted that this on-ground monitoring solution relies on the same measurements (that is, the line-of-sight observations extracted from the images) as the onboard navigation filter. Consequently, the resulting angles-only relative orbit determination is also affected by a weak observability. However, it is possible on ground to use more advanced processing techniques in order to improve

the accuracy and the robustness of the solution: precise post-facto calibration of the maneuvers using the GPS data of the chaser spacecraft, implementation of a batch least-squares estimator to process long data arcs up to several days, and advanced data screening thanks to the usage of multiple iterations. The solution derived on-ground was thus considered as reference throughout the mission to monitor the behavior of the onboard navigation.

The first section of the paper introduces the AVANTI experiment and presents the challenges posed to the relative navigation task. The second section describes the relative navigation system and its two main components: the target detection module and the dynamical filter. The last section presents the flight results.

2. The AVANTI Experiment

2.1. The BIROS Spacecraft

BIROS belongs to the Firebird constellation [2], a DLR small-scale scientific mission primarily meant for Earth-observation and hot-spot detection. It has been launched on the 22nd of June 2016 into an almost-circular, Sun-synchronous orbit characterized by a low altitude. The orbital elements measured after the launch as well as the main spacecraft parameters are summarized in Table 1. The satellite is three-axis stabilized. It makes use of reaction wheels and star trackers to achieve the pointing accuracy required for its main payload (2 arcminutes). The onboard computer is based on an industrial Power PC 823e processor without floating point support and clocked at 48 MHz, yielding a computational speed of 66 MIPS. The star tracker system is based on Micro Advanced Stellar Compass (μASC) devices manufactured by the Danish Technical University (DTU). It features two camera heads and two, cold redundant, digital processing units to deliver the two camera-to-inertial-frame quaternions

Table 1: Relevant mission and spacecraft characteristics

Item	Value	Unit
Semi-major axis	6884	km
Eccentricity	0.0012	-
Inclination	97.5	deg
Right ascension of ascending node	233.6	deg
Argument of perigee	246.3	deg
Mass	140	kg
Dimensions	58 x 88 x 68	cm
Ballistic coefficient	$7.9.10^{-3}$	$m^2.kg^{-1}$
Camera field of view	18.3 x 13.7	deg
Camera resolution	752 x 580	pixel
Camera focal length	20	mm
BEESAT-4 mass	1	kg
BEESAT-4 dimensions	10 x 10 x 10	cm
BEESAT-4 ballistic coefficient	23.10^{-3}	$m^2.kg^{-1}$

at 4 Hz. In addition, it can export pictures with different compression formats.

The AVANTI software has been implemented directly into the onboard computer to have authority on the attitude profile and on the execution of maneuvers. The relative navigation task is designed to process the pictures taken by one of the star trackers. These images are transmitted to the onboard computer through a serial connection, resulting in a reduced data rate (1-2 KB/s). In view of this limitation, the star tracker is configured to transmit only a list of so-called Regions of Interest (ROI). A ROI is a small area of 16x16 pixels centered on a bright object detected in the sky. This compression format allows for a substantial reduction of the picture size. The size of a typical image comprising 60 objects is decreased from 436 kB to only 15 kB. The resulting transfer time to the onboard computer amounts to about 10-15 s, and drives directly the sampling rate of the navigation system (1 picture every 30 s).

As shown in Table 1, the small picosatellite BEESAT-4 ejected by BIROS differs greatly in shape and mass, thus featuring a very different ballistic coef-

ficient b. This value is computed using the following convention:

$$b = C_D \cdot \frac{a}{m} \tag{1}$$

where C_D, a and m denote respectively the drag coefficient, the cross-sectional area and the mass of the spacecraft. An identical value $C_D = 1.3$ has been assumed for both chaser and target.

2.2. Experiment Description

Starting from the in-orbit separation of the BEESAT-4 on September 9, 2016, two months in orbit were necessary for the successful completion of the experiment, most of the time being dedicated to a thorough commissioning of the spacecraft. Dealing with spaceborne autonomous close-proximity formation-flight, it was indeed necessary to ensure that all subsystems involved in the experiment were working properly before starting an autonomous approach. Once the satellite was commissioned, the full featured experiment could start on November 19, 2016, and two autonomous rendezvous were performed at different characteristic ranges. Figure 1 depicts the intersatellite separation during the two autonomous approaches.

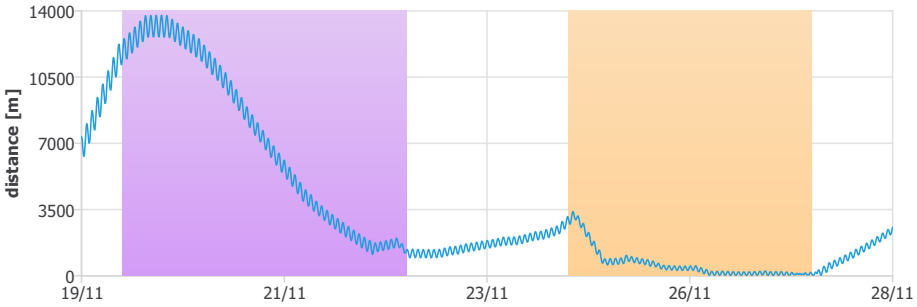

Figure 1: Two autonomous approaches: far to mid range (purple) and mid to close range (orange)

It can be observed in Figure 1 that the distance between the satellites is affected by a sinusoidal pattern. This is due to the fact that, for safety reasons, the approach has been executed in a spiraling fashion as shown in Figure 2. This

peculiar relative motion is the consequence of the adopted passive formation safety concept, which is described more in details in Section 3.5. The onboard autonomous guidance will have the task of reducing step by step the size of the spiral during the approach.

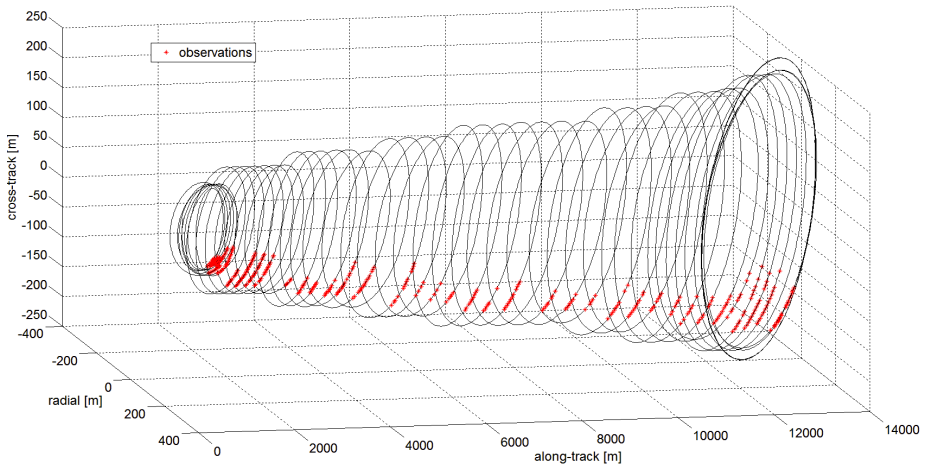

Figure 2: Spiraling approach during the first autonomous approach

The first approach corresponds to the primary objective of AVANTI (that is, the demonstration of far-to-mid range autonomous rendezvous capability). In order to start the experiment, it was required that the target was in the visibility range of the chaser, and that its orbit was coarsely known thanks to the existence of Two-Line Elements (TLEs). In fact, this scenario corresponds to the case in which a coarse orbit phasing has already been performed by the ground segment, based on the knowledge of TLEs of the target. In view of the poor accuracy of the TLEs, a typical safe distance of more than 10 km is usually kept during this preliminary phase. If the initial orbit phasing has been properly done, the size of the relative elliptical motion has already been shrunk enough to be observed completely by simply pointing the camera in the flight direction. Considering a field of view of 18° x 14° (cf. Table 1), this means that the relative elliptical motion should not exceed a size of 3 km x 2.5 km at 10 km distance. This can easily be achieved using a simple ground-in-the-loop

control scheme based on TLEs accurate at the hectometer level. Operationally, the onboard flight software was simply initialized with a coarse a priori relative state derived from the TLEs of BEESAT-4 and had the task to autonomously navigate to the noncooperative traget.

The second approach corresponds to an extension of the experiment. In view of the good system performance observed during the first autonomous approach, it was decided to investigate the extent to which such a relative navigation system could reliably work. This triggered the conduction of the second autonomous approach in order to explore the limits of line-of-sight navigation. Further details about the objectives and design of the experiment can be retrieved in Reference [1].

AVANTI presents a unique opportunity to experimentally investigate how different disturbances (which are otherwise difficult to faithfully simulate) impact the autonomous vision-based rendezvous system. Among the numerous challenges and constraints encountered during experiment, the navigation specifically had to face the following issues:

- Contrary to ARGON which, thanks to the dusk-dawn orbit of PRISMA, benefited from optimal illumination conditions, AVANTI deals with target objects flying on any kind of low Earth orbits. This has dramatic impacts in terms of visibility since on one hand the target object is eclipsed during a large part of the orbit and on the other hand the camera becomes blinded by the Sun during another large part of the orbit. As a result, only a tiny portion of the relative motion is visible. Figure 2 provides a clear illustration of the poor visibility conditions where the red sections of the trajectory represent the line-of-sight measurements which were available during the approach.

- BIROS is equipped with one single cold-gas thruster which needs to be oriented and kept in the proper direction for a long time depending on the size of the maneuver. The BIROS attitude controller was not always able to accurately keep the desired attitude (exhibiting control errors up to

several degrees). This resulted in large maneuver execution errors which added even more uncertainties to the onboard relative motion model.

- Finally, BIROS flies at a low altitude inducing a strong unknown differential drag which has to be estimated as part of the navigation process. The simulations had indicated that this would be possible under the assumption that the unknown differential drag would have a similar pattern over large time scales.

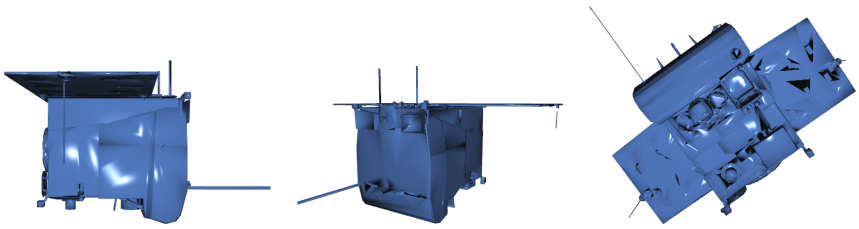

(a) Earth-pointing (b) Target-pointing (c) Cooling down

Figure 3: Cross-sectional area for different attitude modes

This assumption revealed itself to be wrong in view of the frequent switches of attitude mode resulting in large variations of the spacecraft cross-sectional area (as shown in Figure 3) and in dramatic changes of the differential drag acting on the satellite. During the experiment, it was often necessary to point the antennas to the ground stations for high-speed data transmission, to orient the thruster to the desired direction of the maneuvers and to enter a special satellite cool-down attitude to cope with unexpected thermal problems [1]. Note that the attitude of the noncooperative target spacecraft also influences the differential drag but was unknown during the experiment.

3. Angles-Only Relative Navigation Filter

3.1. System Overview

The vision-based relative navigation system presented in this paper is designed to be used by a chaser spacecraft to approach a known noncooperative object, referred to here as the target object. As a consequence, it is assumed that the orbit of the target is coarsely known (for example using ground-based radar tracking) and that the chaser is flying on a similar orbit. The relative navigation task consists of continuously providing an estimate of the state of the formation in real-time to the other onboard applications (guidance, control, attitude pointing). Since the star trackers are the only sensors available for relative navigation, this estimation is derived from line-of-sight measurements which first have to be extracted from the images taken by the camera. In view of the desired working range, all the objects imaged by the camera are considered as point sources.

Figure 4 depicts the task flow of the vision-based navigation system. In a first step, a raw image is processed to extract a collection of luminous spots after a threshold-filtering of the background noise (**image segmentation**). Afterward, the center of the spots is estimated by computing the arithmetic mean of the pixels (**centroiding**). At this stage, the raw image has been simplified to a list of so-called centroids, the majority of them corresponding to stellar objects.

The next step consists in identifying these stellar objects (**star identification**) in order to derive the precise orientation of the camera. In principle, this could be done without any external help using a lost-in-space algorithm to recognize the stars. Such algorithms are typically implemented in star trackers, in order to identify the stars using only their angular distance. For simplicity, it has been decided to rely instead on the onboard knowledge of the spacecraft attitude (accurate to a few arcminutes) to first identify the stellar objects. In a second step, the knowledge of the orientation of the camera is refined (reaching an accuracy of a few arcseconds) using the q-method [22] (**attitude estimation**).

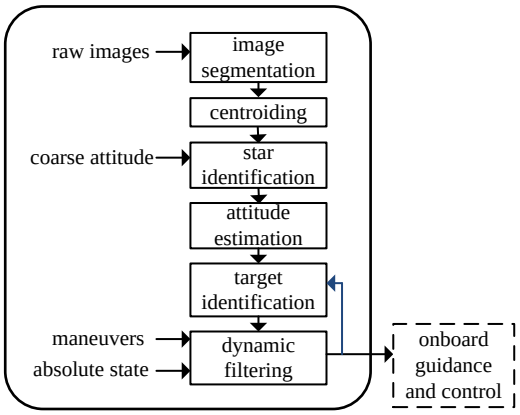

Figure 4: Functional view of the vision-based relative navigation system

The four above-mentioned tasks belong to star tracker technology and are thus not detailed here. The contribution of the paper lies rather in the design of a simple, robust and accurate relative navigation algorithm composed of a **target identification** module associated to a **dynamic filtering** of the relative motion. The target detection module aims at recognizing an object flying on a similar orbit based on its apparent trajectory which differs greatly from the trajectories of other satellites. This technique is named kinematic target detection. The relative state estimate might also be used for the detection of the target after the filter convergence. This feature is represented by a blue arrow in Figure 4 and is named dynamic target detection.

Once the target has been recognized, the navigation filter processes these observations and, thanks to the knowledge (provided externally) of the absolute state and maneuvers executed by the chaser spacecraft (i.e, BIROS), derives the relative state estimate.

3.2. Robust Target Identification

One of the main challenges faced by an autonomous vision-based navigation system is the ability to provide reliable line-of-sight measurements to the navigation filter. To do this, the measurements have to be extracted from the star tracker pictures, requiring the capability to identify the target object among all

the luminous spots present in the image. As depicted in Figure 5, it is from far range no possible to distinguish at one glance the target satellite from the other objects imaged by the camera.

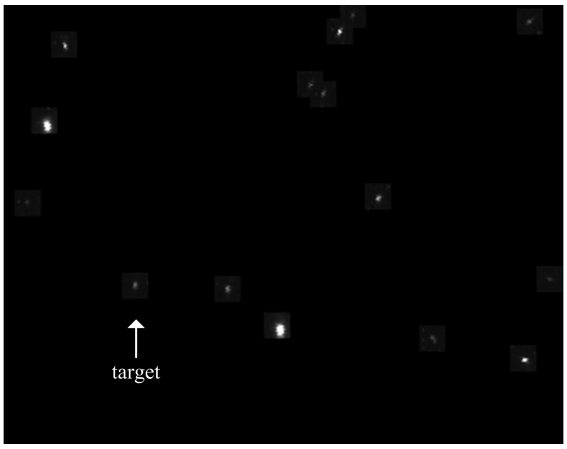

Figure 5: On the difficulty to recognize a target satellite at 30 km distance (image from the ARGON experiment).

Most of the celestial objects can of course be identified using a star catalog during the previous star identification process (see Section 3.1). Still it cannot be excluded that several non-identified luminous spots remain. The object recognition task can be degraded for several reasons:

- a spot corresponds to a celestial object which is not present in the onboard catalog
- a spot is not a celestial object (e.g. other satellite, debris, asteroid,...)
- a spot corresponds to a defect of the camera sensor (hot spot).

In order to select the target satellite among several candidates which are not recognized as stellar objects, additional knowledge about the target satellite is required. To that end, it is tempting to use the current onboard relative state estimate. However, this approach is considered dangerous because the target identification relies on the information provided by the navigation filter, and can thus search in the wrong direction if the state estimate is affected by some

errors. Similarly, the apparent magnitude of the object cannot be exploited at far range, because it strongly depends on the unknown attitude of the target satellite and on the illumination conditions (cf. Figure 6).

Figure 6: Example of variation of luminosity during one orbit at 28 km distance (image from the ARGON experiment).

As a result, it has been decided to use a pure kinematic approach to identify the possible targets and to use the luminosity information only if there is a need to discriminate between several candidates. The retained strategy for robust target identification is based on the fact that, when flying on a similar orbit, the apparent motion of the target object differs completely from the apparent motion of unrecognized stellar objects or non-stellar objects flying on different orbits, making it possible to recognize the target object form this peculiar trajectory. The trajectory detection algorithm is described in the following section.

3.3. Extraction of the Trajectory

The objective of the algorithm is to recognize a trajectory throughout a sequence of images. Once the stars have been recognized, the remaining unidentified centroids are the target satellite itself as well as other possible non-celestial objects, unrecognized stars and camera anomalies like hot spots. By combining several images, it becomes possible to distinguish clearly the trajectory of the target object surrounded by additional centroids and thus to isolate this trajectory using a clustering algorithm. The Density-Based Spatial Clustering of Applications with Noise (DBSCAN) algorithm [23] has been retained for this purpose. DBSCAN groups points into clusters depending on the distance to their neighbors and on the number of neighbors. In addition to its simplicity of implementation, the algorithm presents three major advantages:

- it does not require any a-priori knowledge on the number of clusters and their shape
- it requires only two parameters (the maximum distance ϵ to the neighbors and the minimum number of neighbors $n_{\min}$ to be included in the cluster)
- it has a notion of noise, which means that an isolated point is not associated to any cluster.

This latter characteristics makes this algorithm particularly suited for the detection of a target flying on a similar orbit. As a rule of thumb, two orbits can be considered similar when the magnitudes of the relative position and velocity vectors are smaller than 1% of the absolute ones. In this case, when pointing the camera in the direction where the target is expected to be visible, the target displacement between two images is very small compared to the apparent displacement of an unrecognized star or another satellite flying on a different orbit between the same time interval. Consequently, the unrecognized objects are likely to be considered as noise. Figure 7 illustrates this idea by showing a sequence of six images in which the trajectory of the target spacecraft (in green) is clearly recognizable as well as the trajectories of two unrecognized stars (represented by a dashed line). In this example, the clustering algorithm builds three clusters (in green, red, and blue) based on the spatial distribution of the points and considers the other points as noise (in white).

It has to be noted that some (very) coarse a-priori knowledge on the target relative orbit is needed to tune the DBSCAN algorithm. The displacement between two consecutive pictures depends on the size of the relative elliptic motion and on the distance to the target (this information is provided to initialize the filter afterward). If the displacement between two images is set too small, it would result in the target trajectory being discarded as noise in the DBSCAN algorithm, while setting it too big would include unnecessary unrecognized objects to the target trajectory. As rule of thumb, it is enough to consider that the target travels the size of the relative elliptic motion in half-an-orbit, so that the expected angular displacement can be roughly estimated as follows: if n, d,

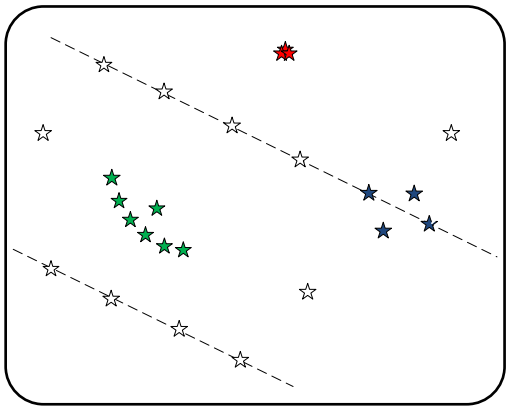

Figure 7: Detection of clusters in a sequence of pictures.

h and T denote respectively the chaser mean motion, the distance to the target spacecraft, the cross-sectional size of the relative elliptic motion (cf. Figure 8) and the time interval between two pictures, a very coarse approximation of the angular distance β traveled by the target between two pictures is

$$\beta = \tan \frac{h}{d} \cdot \frac{n}{\pi} T \tag{2}$$

which can be translated into a distance ϵ in pixels using the camera field of view F and resolution R:

$$\epsilon = \beta \cdot \frac{R}{F} \tag{3}$$

Since all quantities are rough approximations, one may use a multiple of ϵ (for example 2ϵ or 3ϵ) to be on the safe side.

At this stage, several clusters are still competing. In the example depicted in Figure 7, the green cluster matches the target trajectory, but another unrecognized object (in green) has been added to the cluster and clearly does not belong to the trajectory. The red cluster is composed of hot spots and the blue cluster is the result of the random conjunction of unrecognized objects (for example due to a passing-by satellite). In order to discriminate the target trajectory, the target identification algorithm relies on the fact that the relative motion of

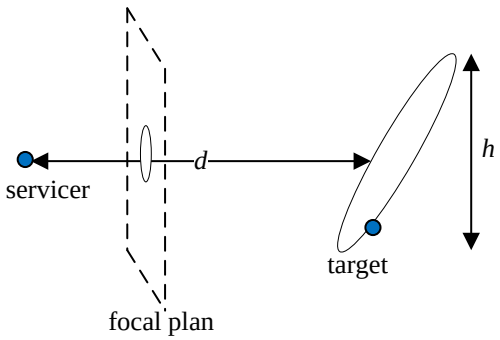

Figure 8: Relative elliptic motion.

the spacecraft follows predictable space dynamics. The projection of its elliptic trajectory on the focal plane can thus be easily recognized. The algorithm attempts to identify this trajectory by fitting each cluster with a second order Bezier curve. The choice of a Bezier curve is motivated by the simplicity of its formulation and its ability to approximate a portion of trajectory projected on a plane. Mathematically the Bezier curve $\boldsymbol{B}(\tau)$ is parameterized by a variable τ and defined by a set of three two-dimensional control points $\boldsymbol{P}_0$, $\boldsymbol{P}_1$, and $\boldsymbol{P}_2$:

$$\boldsymbol{B}(\tau) = (1-\tau)^2\boldsymbol{P}_0 + 2\tau\boldsymbol{P}_1 + \tau^2\boldsymbol{P}_2, \tau \in [0,1] \tag{4}$$

In view of the simple formulation of Eq. 4, the curve fitting is trivial and can be done using a least-squares approach. Here the parameter τ has to reflect the fact that the trajectory is a time-dependent suite of points. This can be achieved by considering the timestamp t_k of the points composing the cluster returned by the DBSCAN algorithm. If $t_{\min}$ and $t_{\max}$ denote respectively the oldest and newest timestamps of the set of points composing the cluster, the parameter τ_k associated to the point stamped with the time t_k can be defined as

$$\tau_k = \frac{t_k - t_{\min}}{t_{\max} - t_{\min}} \tag{5}$$

so that the oldest point will be associated with $\tau = 0$ and the newest point

with $\tau = 1$ The algorithm selects only the clusters which could be successfully fitted, based on the curve fitting residuals σ_B. Considering typical centroiding errors of less than half a pixel and the fact that the Bezier curve is only an approximation of the real trajectory, the algorithm considers a fitting successful if $\sigma_B < 1$ pixel.

3.4. Final Integrity Check and Aided Target Selection

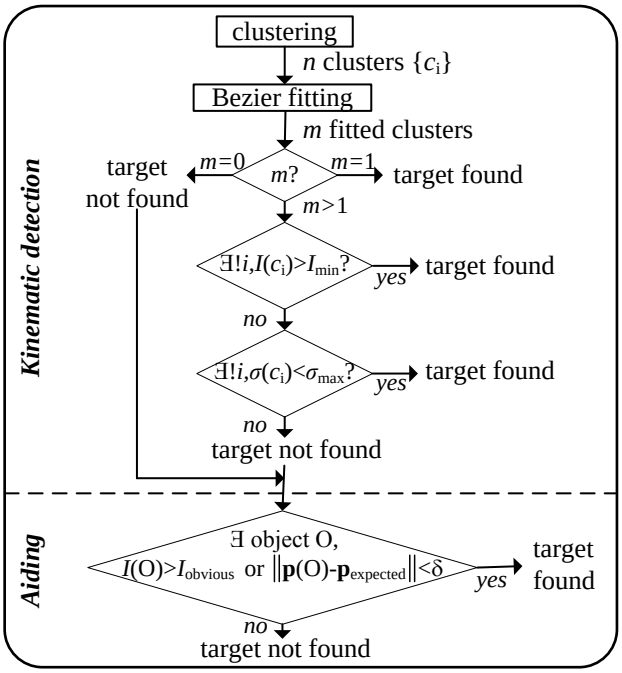

Figure 9: Functional view of the target detection algorithm.

The strategy described above works well to find the candidate trajectories and to reject clusters made of the conjunction of random unrecognized objects (for example to reject the blue cluster in Figure 7), but might however fail in some rare cases if the cluster elements are too close to each other to allow for an obvious discrimination based only on the curve fitting residuals. This situation can, for example, occur in the case of hot spots, which are always located at same position with small variations due to the centroiding errors. Hot spots

are pixels with abnormally high dark current. They represent a threat for the robustness of the target identification algorithm because they can hardly be distinguished from the target object at far range. It has to be emphasized that hot spots should be catalogized as part of the calibration phase. However, the target identification algorithm needs to be robust to undetected hot spots during the calibration phase or to new hot spots appearing on-orbit.

Some countermeasures, depicted in Figure 9, can help mitigate this issue. The most evident criteria to select the target trajectory in case of doubt is to use the object luminosity, since a hot spot affects only one pixel and the target image is spread over many pixels (at least 2 or 3 pixels at far-range). This is due to the fact that the optics of the camera is slightly defocused for better centroiding performance so that even an object of low visual magnitude is composed of several pixels. Thus, the centroiding function is designed to deliver (in addition to the estimated center) the luminosity I of the centroid, which is simply the sum of the values of the pixels belonging to the centroid (note that in Figure 9, $I(c_i)$ means the intensity of the most recent element of a cluster c_i describing a trajectory). The camera retained for AVANTI encodes the pixels using a single byte, so their value is comprised between 0 and 255. Accordingly, it can be assumed that the intensity of a hot spot will be much smaller than $I_{\min}= 1000$ (in fact 255 should be enough, but some neighboring pixels might sometimes contribute to increase the measured brightness of the hotspot).

However, at far-range, it might be that the target satellite also occupies very few pixels, so that its luminosity is very close to that of a hot spot. In this case, it is helpful to remember that the distribution of the elements comprising the target follows a trajectory while the elements of the hot spots are randomly distributed, so that a small but observable difference in terms of fitting residuals will still be observable. At far-range, the advantage is that the centroiding errors are particularly small (approximately 0.2-0.3 pixel) since the object can be considered as a point source at this distance. Consequently, the fitting residuals of the target trajectory will also be particularly small, while the fitting residuals of a cluster of hot spots will be slightly larger due to the random distribution

of the hot spots over time. This statement is no longer valid at mid-range because the distribution of the pixels composing the target image cannot be considered as a point spread function anymore, resulting in higher centroiding errors. Figure 19 of Section 4.2 provides an example of the target image at different separations. The increasing centroid errors impact the curve fitting residuals, but this is not a problem since the target luminosity can then be used to discriminate the candidates.

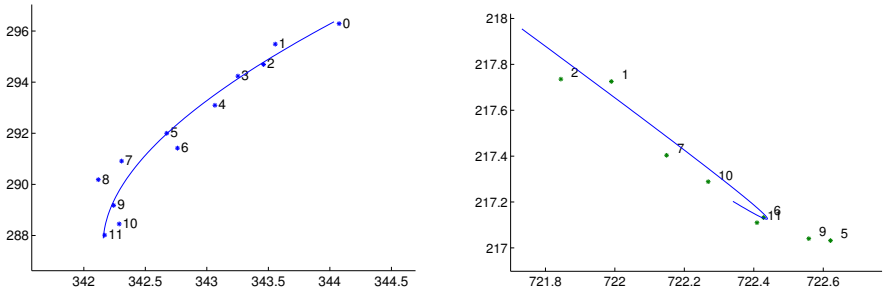

(a) Target trajectory (σ_B=0.21 pixel) (b) Hot spot (σ_B=0.39 pixel).

Figure 10: Examples of Bezier fitting (from the PRISMA mission during the ARGON experiment).

Figure 10 shows as examples two Bezier curve fittings, corresponding to the target trajectory and a randomly distributed collection of centroids corresponding to a single hot spot over a sequence of images. The axis coordinates of Figure 10 correspond to the position in pixels in the focal plane and the number k close to the points indicates their index in the sequence of N images ($k = 0$ corresponds to the oldest image and $k = N - 1$ to the most recent one). Since the parameter τ of the Bezier curve is chosen to follow the picture index (i.e., $\tau = \frac{k}{N-1}$), a series of points which are not properly ordered will be more difficult to fit (cf. Figure 10(b)) . It has to be noted that this strategy excludes the possibility for the camera to actively follow the target spacecraft at far-range, otherwise both the target and hot spot describe a similar apparent motion and cannot be distinguished from their luminosity (this problem disappears at mid- and close-range because the target becomes more luminous).

The kinematic target detection is best suited for initiating the approach at far-range when little knowledge about the relative orbit is available. Once the filter has converged, the dynamical solution can advantageously be used to support this task. In this case, a predicted target position in the image can be derived from the filter relative state. If a non-identified centroid is sufficiently close to the modeled position (within a tolerance derived from the covariance matrix), the centroid is identified as target. Similarly, at close-range, the considerable brightness of the target allows for an unambiguous detection. Both criteria are summarized in Figure 9: if the kinematic detection fails, the target detection can be aided by scanning all the objects $\mathcal{O}$ in the image and checking if the luminosity of a non-recognized object is greater than an obvious luminosity threshold I_{obvious} or if its expected position $\boldsymbol{p}$ in the picture is close enough (less than a user-defined search radius δ) to the image position $\boldsymbol{p}_{\text{expected}}$ predicted by the filter navigation solution. I_{obvious} is empirically set to 10000, which corresponds to a square of 6x6 saturated pixels. This value has been derived considering the hardware specifications of the camera employed for AVANTI. At far-range, when the exposure time of the camera is set to 0.25 s, this value corresponds to the brightness of a star of magnitude 1. At mid- to close-range, the electronic shutter of the camera adjusts the exposure time to keep the image of an object into a ROI (i.e, a 16x16 pixel large area as explained in Section 2.1.). In this case, I_{obvious} corresponds to a bright object occupying 15% of the ROI (see Figure 19 for some examples of ROIs at close-range).

3.5. Dynamical Filtering

Once the line-of-sight measurements are extracted from the images, the relative state of the formation can be estimated using a dynamical filter. The onboard filter is based on a special parametrization of the relative motion, described by a set of dimensionless relative orbital elements $\boldsymbol{\delta\alpha}$ [24]:

$$\delta\boldsymbol{\alpha} = \begin{pmatrix} \delta a & \delta e_x & \delta e_y & \delta i_x & \delta i_y & \delta u \end{pmatrix}^T, \tag{6}$$

where δa is the relative semi-major axis, $\delta\boldsymbol{e} = \left(\delta e_x, \delta e_y\right)^T$ and $\delta\boldsymbol{i} = \left(\delta i_x, \delta i_y\right)^T$ are called respectively relative eccentricity and inclination vectors, and δu stands for the relative mean argument of latitude. Note that δu is sometimes equivalently replaced in the literature by the relative mean longitude $\delta\lambda = \delta u + \text{cotan}(i) \cdot \delta i_y$, where i represents the orbit inclination. As depicted in Figure 11 the relative orbital elements are used to describe the state of the formation and can easily be translated in a Cartesian representation if needed. In Figure 11, the unit vectors $\boldsymbol{e}_\text{R}$, $\boldsymbol{e}_\text{T}$ and $\boldsymbol{e}_\text{N}$ are aligned with the Radial, Tangential, and Normal directions of the local comoving orbital frame denoted $\mathcal{F}$. Mathematically, the cartesian relative position $\delta\boldsymbol{r}^{\mathcal{F}}$ in the frame $\mathcal{F}$ is described by [24]:

$$\delta\boldsymbol{r}^{\mathcal{F}} = \begin{pmatrix} 1 & -\cos u & -\sin u & 0 & 0 & 0 \\ 0 & 2\sin u & -2\cos u & 0 & \cot i & 1 \\ 0 & 0 & 0 & \sin u & -\cos u & 0 \end{pmatrix} \cdot \delta\boldsymbol{\alpha} = \boldsymbol{\Gamma} \cdot \delta\boldsymbol{\alpha} \quad (7)$$

Eq. 7 shows that the in-plane relative motion is described by δa, $\delta\boldsymbol{e}$ and δu whereas $\delta\boldsymbol{i}$ is responsible for the cross-track motion.

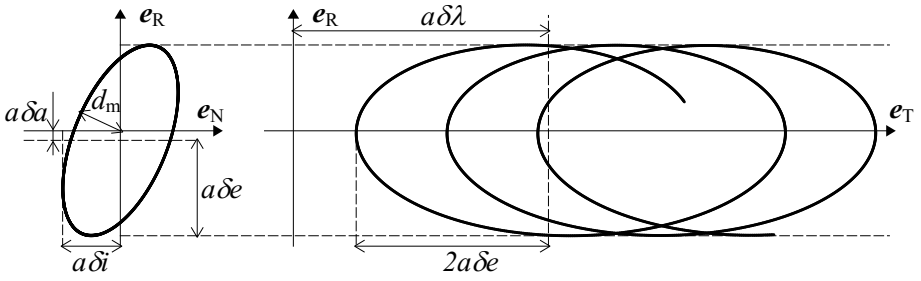

Figure 11: Relative motion (target with respect to chaser) in the local orbital frame. A small non-vanishing δa is responsible for a drifting relative orbit.

As already emphasized in the past[25], this parametrization is of great interest when dealing with formations of satellites since it offers a quick insight into the geometry of the relative motion and a simple criteria to guarantee the safety of the formation. Provided that $\delta\boldsymbol{e}$ and $\delta\boldsymbol{i}$ are parallel, it can be ensured that the intersatellite distance in the Radial-Normal plane will always stay above a

minimum value d_m, as seen in Figure 11. This criteria is valid only for small differences in semi-major axis (typically less than 10% of $\min(\|\delta\boldsymbol{e}\|, \|\delta\boldsymbol{i}\|)$), since a non-vanishing δa shifts the relative elliptical motion in the radial direction, thus decreasing the minimum distance d_m. For embedded onboard systems, the major advantage of this parameterization lies in the associated analytical dynamical model, which provides an accurate and computationally-light prediction of the relative motion thanks to the inclusion of the perturbation due to the Earth's oblateness (J_2). Mathematically, the model relates the state $\delta\boldsymbol{\alpha}$ of the formation at time t to the state at epoch t_0 by the means of the state transition matrix $\boldsymbol{\Phi}$:

$$\delta\boldsymbol{\alpha}(t) = \boldsymbol{\Phi}(t - t_0) \cdot \delta\boldsymbol{\alpha}(t_0) \tag{8}$$

This analytical model has been notably successfully employed to design the previous DLR's spaceborne autonomous formation-flying experiments implemented on the TanDEM-X [26] and PRISMA [27] satellites. The formation used for the AVANTI experiment undergoes a much stronger differential drag due to its low altitude and to the very different ballistic coefficients of BIROS and BEESAT-4 (see Table 1). As a result, the relative motion model has been revisited during the design of the AVANTI experiment to refine the modeling of the disturbance due to J_2 and to include the mean effects of the differential drag [28]. Since this latter perturbation is extremely difficult to model accurately, it has been decided for simplicity to make use of external empirical values describing the resulting time variations of δa and $\delta\boldsymbol{e}$, which are approximated to constant values. The refined dynamical model thus takes three additional parameters ($\delta\dot{a}$, $\delta\dot{e}_x$, $\delta\dot{e}_y$) and becomes:

$$\delta\boldsymbol{\alpha}(t) = \boldsymbol{\Phi}(t - t_0, \delta\dot{a}, \delta\dot{e}_x, \delta\dot{e}_y) \cdot \delta\boldsymbol{\alpha}(t_0) \tag{9}$$

The autonomy of the system would however suffer from the external manual input of these additional parameters. They have thus to be estimated onboard. However the weak observability of the problem makes it dangerous to estimate too many additional parameters, which may degrade the robustness of the solution. As a result, it has been decided to estimate only $\delta\dot{a}$, thus neglecting the

impact of the differential drag on $\delta \boldsymbol{e}$ (which is smaller than the effect on δa). The state vector describing the formation which has to be estimated onboard can thus be written as:

$$\boldsymbol{x} = \begin{pmatrix} \delta \boldsymbol{\alpha}^T & \delta \dot{a} \end{pmatrix}^T, \tag{10}$$

and according to Reference 28 the associated state transition matrix $\tilde{\boldsymbol{\Phi}}$ becomes (note that the order of the components of $\delta \boldsymbol{\alpha}$ differs from Reference 28):

$$\tilde{\boldsymbol{\Phi}}(t-t_0) = \begin{pmatrix} 1 & 0 & 0 & 0 & 0 & 0 & dt \\ 0 & 1 & -\dot{\varphi}dt & 0 & 0 & 0 & 0 \\ 0 & \dot{\varphi}dt & 1 & 0 & 0 & 0 & 0 \\ 0 & 0 & 0 & 1 & 0 & 0 & 0 \\ (21/4)\gamma \sin(2i)ndt & 0 & 0 & 3\gamma(\sin^2 i)ndt & 1 & 0 & (21/8)\gamma \sin(2i)ndt^2 \\ -(3/2)ndt & 0 & 0 & -(3/2)\gamma \sin(2i)(5+3\eta)ndt & 0 & 1 & -(3/4)ndt^2 \\ -(21/4)\gamma(K+H\eta)ndt & & & & & & -(21/8)\gamma H(\eta+1)ndt^2 \\ 0 & 0 & 0 & 0 & 0 & 0 & 1 \end{pmatrix} \tag{11}$$

According to Reference 28, the variables used in Eq.11 are defined as follows:

$$\begin{array}{lll} n = \sqrt{\mu_\oplus / a^3} & \eta = \sqrt{1-e^2} & \gamma = \dfrac{J_2}{2}\dfrac{R_\oplus^2}{a^2\eta^4} \\ H = (3\cos^2 i - 1) & K = (5\cos^2 i - 1) & D = \dfrac{6K}{\eta^2} + \dfrac{9H}{2\eta} \\ dt = (t - t_0) & \varphi' = (3/2)\gamma K & \dot{\varphi} = n\varphi', \end{array} \tag{12}$$

where a and e denote respectively the semi-major axis and eccentricity of the chaser orbit.

In view of the real-time requirements, an Extended Kalman Filter (EFK) as been chosen as an estimator. The time update at each new epoch t is done using the state transition matrix of Eq. 11. The maneuvers executed by the chaser are crucial to improve the observability. In the filter design, they are considered impulsive and are included as part of the time update process. If $\delta \boldsymbol{v}$ denotes a

velocity increment executed at argument of latitutde u_M and expressed in the frame $\mathcal{F}$, it can be shown [24] that the resulting change of the relative orbital elements $\Delta\delta\boldsymbol{\alpha}$ is:

$$\Delta\delta\boldsymbol{\alpha} = -\frac{1}{n} \cdot \begin{pmatrix} 0 & 2 & 0 \\ \sin u & 2\cos u & 0 \\ -\cos u & 2\sin u & 0 \\ 0 & 0 & \cos u \\ 0 & 0 & \sin u \\ -2 & 0 & -\sin u \cot i \end{pmatrix} \tag{13}$$

The filter measurement update is done using the line-of-sight measurement $\boldsymbol{\rho}$ to the target object. This observation is done in the camera frame, denoted $\mathcal{C}$. Since the target detection provides a pixel position $\boldsymbol{p}$ corresponding to the center of mass of the target, it is first necessary to convert it into a line-of-sight measurement using a camera model $\boldsymbol{g}$:

$$\boldsymbol{\rho} = \boldsymbol{g}^{-1}(\boldsymbol{p}) \tag{14}$$

The camera model $\boldsymbol{g}$ (mapping a unit vector into a pixel position) is a pinhole camera model complemented with lens distortion [29]. The line-of-sight can be written using the relative position in the camera frame $\delta\boldsymbol{r}_{\mathcal{C}}$:

$$\boldsymbol{\rho} = \frac{\delta\boldsymbol{r}^{\mathcal{C}}}{\|\delta\boldsymbol{r}^{\mathcal{C}}\|} = \frac{\boldsymbol{R}^{\mathcal{C}}_{\mathcal{F}}\delta\boldsymbol{r}^{\mathcal{F}}}{\|\delta\boldsymbol{r}^{\mathcal{F}}\|} = \frac{\boldsymbol{R}^{\mathcal{C}}_{\mathcal{F}}\boldsymbol{\Gamma}\delta\boldsymbol{\alpha}}{\|\boldsymbol{\Gamma}\delta\boldsymbol{\alpha}\|} \tag{15}$$

Here $\boldsymbol{R}^{\mathcal{F}}_{\mathcal{C}}$ denotes the rotation matrix from the frame $\mathcal{C}$ to the frame $\mathcal{F}$ and is delivered by the image processing task (as part of the precise star-based estimation of the orientation of the camera, cf. 4). The line-of-sight vector $\boldsymbol{\rho}$ is parameterized by a set of two angles A and E, corresponding respectively to the azimuth and elevation in the camera frame:

$$\boldsymbol{\rho} = \begin{pmatrix} \cos(E)\sin(A) \\ \sin(E) \\ \cos(E)\cos(A) \end{pmatrix} \tag{16}$$

These two angles are used to build the measurement vector $\boldsymbol{z} = \begin{pmatrix} A & E \end{pmatrix}^T$ used for the measurement update. The related Jacobian matrix $\boldsymbol{H}$ is computed

considering the different frames used to derive the equations:

$$\boldsymbol{H} = \frac{\partial \boldsymbol{z}}{\partial \boldsymbol{x}} = \frac{\partial \boldsymbol{z}}{\partial \delta \boldsymbol{r}^{\mathcal{C}}} \cdot \frac{\partial \delta \boldsymbol{r}^{\mathcal{C}}}{\partial \delta \boldsymbol{r}^{\mathcal{F}}} \cdot \frac{\partial \delta \boldsymbol{r}^{\mathcal{F}}}{\partial \boldsymbol{x}} = \frac{\partial \boldsymbol{z}}{\partial \delta \boldsymbol{r}^{\mathcal{C}}} \cdot \boldsymbol{R}_{\mathcal{F}}^{\mathcal{C}} \cdot \frac{\partial \delta \boldsymbol{r}^{\mathcal{F}}}{\partial \boldsymbol{x}}, \tag{17}$$

In the formulation of the Jacobian, $\frac{\partial \delta \boldsymbol{r}^{\mathcal{F}}}{\partial \boldsymbol{x}}$ is computed according to Eq. 7, and noting that the relative position does not depend on $\delta \dot{a}$:

$$\frac{\partial \delta \boldsymbol{r}^{\mathcal{F}}}{\partial \boldsymbol{x}} = \Big(\boldsymbol{\Gamma} \mid 0_{3x1} \Big) \tag{18}$$

The partial derivatives of the measurements with respect to the relative position in the camera frame are finally given by:

$$\frac{\partial A}{\partial \delta \boldsymbol{r}^{\mathcal{C}}} = \frac{1}{\delta r \cos^2(E)} \cdot \Big(\cos A \cos E \quad 0 \quad -\cos E \sin A \Big) \tag{19a}$$

$$\frac{\partial E}{\partial \delta \boldsymbol{r}^{\mathcal{C}}} = \frac{1}{\delta r} \cdot \Big(-\sin E \sin A \quad \cos E \quad -\sin E \cos A \Big) \tag{19b}$$

3.6. Filter Tuning

Compared to other estimation techniques (for instance least-squares adjustment), the Kalman filter offers the advantage of using process noise to cope with the errors of the dynamical model. This is of great importance since, in addition to the errors due to the differential drag, the filter has to cope with maneuver execution errors. On the other hand, the improvement of observability is obtained by considering the effect of maneuvers over time, requiring thus some filter memory, which fades quickly when introducing too much process noise. A tradeoff needs to be found between these contradictory statements.

The poor observability and the unknown perturbations of the relative dynamics make the proper tuning of the filter not trivial. In principle, dedicated process noise should be introduced when executing the maneuvers, corresponding to the execution errors. However, numerical simulations have shown that this strategy weakens the observability, preventing the filter convergence. It has been found more robust to consider a global constant value for the process

noise, reflecting the average uncertainties of the relative dynamics. An order of magnitude for the contribution of the unknown differential drag can be derived considering an atmopheric density of 5 g/km^3 at about 500 km altitude, yielding a relative acceleration of about 200 nm/s^2 for a differential ballistic coefficient of 0.015 m^2/kg. Since the sampling time of the filter is chosen according to the frequency of measurements, i.e. 0.033 Hz or 1 image every 30 s, this perturbation corresponds to a tangential velocity increment of 6 μm/s over 30 seconds. The overall contribution of the maneuver execution errors can be coarsely assessed by allocating a total error of 10 mm/s spread over one day (considering an average of 5 maneuvers affected by 2 mm/s errors), contributing to an average of 3 μm/s over 30 s. According to Eq. 13, this total unknown $\delta\boldsymbol{v}$ of 9 μm/s translates into 1-2 cm error depending on the direction and location of the velocity increment. It has also to be noted that the influence of the drag on the relative eccentricity vector $\delta\boldsymbol{e}$ has been neglected in the relative motion model while the mean effect of this perturbation on δa is estimated by the filter, thus reducing the errors of the dynamics for this particular component. Consequently, it has been decided during the tuning of the filter to reduce the uncertainty affecting δa. The filter settings retained for the experiment are summarized in Table 2:

Table 2: Adopted filter settings

Item	Value
A-priori state error	diag(10,100,100,100,100,500,10^{-4})
Process noise	(10^{-4},0.03,0.03,0.03,0.03,0.1,10^{-7})
Measurement noise	80 arcsec

There still exists room for improvement for the filter design. The weak observability, the model deficiencies and the introduction of process noise make the filter prone to instability. During AVANTI, the a-priori covariance matrix has been reduced on purpose to avoid any filter divergence, and the behavior of the filter has been closely monitored during the two autonomous approaches. Thus the covariance described in Table 2 is not really representative of the accuracy of TLEs, which can amount to several hundred meters [30].

4. Flight Results

4.1. Far to Mid Range Autonomous Approach

The first autonomous approach represents the core of the AVANTI demonstration. As already mentioned, the main difficulty at far-range lies in properly recognizing the target. The TLEs are of little help, since their large cross-track error (up to a few hundred meters) does not significantly reduce the target search area in the image, so that many candidate target objects can be simultaneously visible. A kinematic trajectory analysis is thus the preferred method for the target detection when initiating the approach; however, this is not a trivial activity considering the few available pictures. Figure 12 depicts the difficulty of this task by focusing on the first hours after the start of the autonomous rendezvous. In Figure 12, the total number of centroids visible in the images are drawn in blue, while the centroids which have not been identified as stars are shown in red. Here again, the limited number of measurements is clearly visible: the gray areas represent the eclipse phases, during which the target is not visible, and the remaining areas without centroids correspond to the phases where the camera was blinded by the Sun.

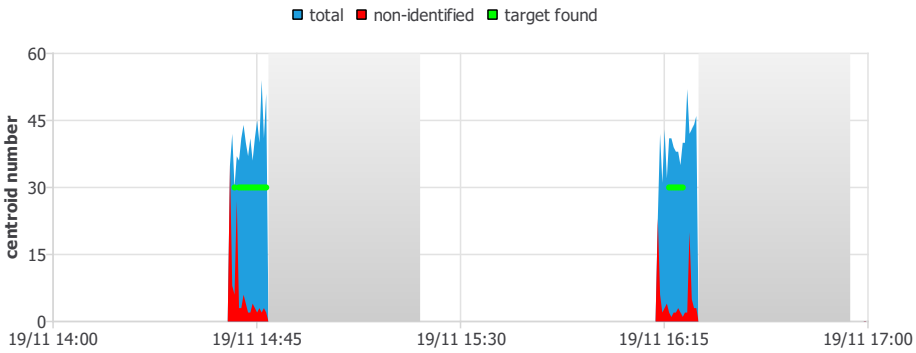

Figure 12: Centroids detected and identified at 13 km distance

As a result, only approximately 10 minutes of pictures are remaining every orbit, from which the target has to be identified. Figure 12 shows that the number of unrecognized objects is slightly greater than one with some unexpected

peaks where the satellite onboard attitude estimation is too degraded to allow for the proper detection of the stars. Nevertheless, despite these anomalies, the strategy adopted for target detection was robust enough to successfully detect the picosatellite (green dots in Figure 12). Note that the detection is not immediate since the algorithm first needs to collect a sequence of images to be able to detect a candidate trajectory.

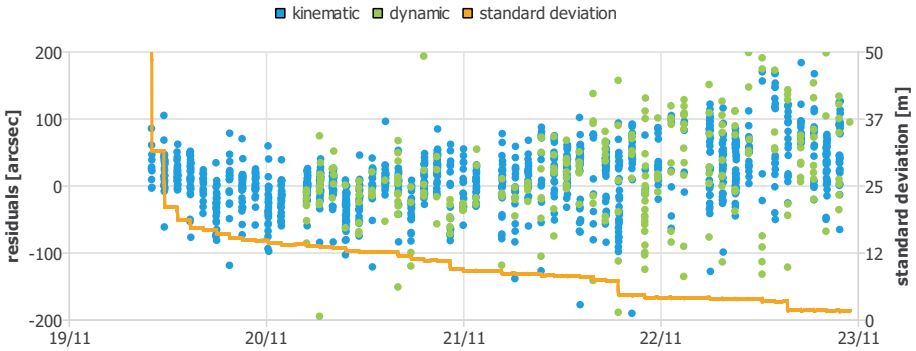

Figure 13: Filter residuals

Once a few line-of-sight observations are successfully extracted from the images, the filter refines its coarse a priori knowledge of the relative state until it gains enough confidence about the validity of its solution (the filter is considered to have converged if the standard deviation of the solution decreases to below a user-defined threshold). From this moment, the filter state can be used to support the target detection, thus providing more measurements. This behavior is illustrated in Figure 13, where the filter residuals have been plotted during the complete approach. Note how new measurements gained with a dynamic detection appear (in green) once the standard deviation decreases under 13 m (the standard deviation has been computed excluding $a\delta u$ to provide a measure of the lateral accuracy). A clear degradation of the residuals depending on the distance can be observed (the intersatellite separation decreases continuously during the approach, cf. Figure 1), this aspect will be even more pronounced at close-range and will be treated in the next section.

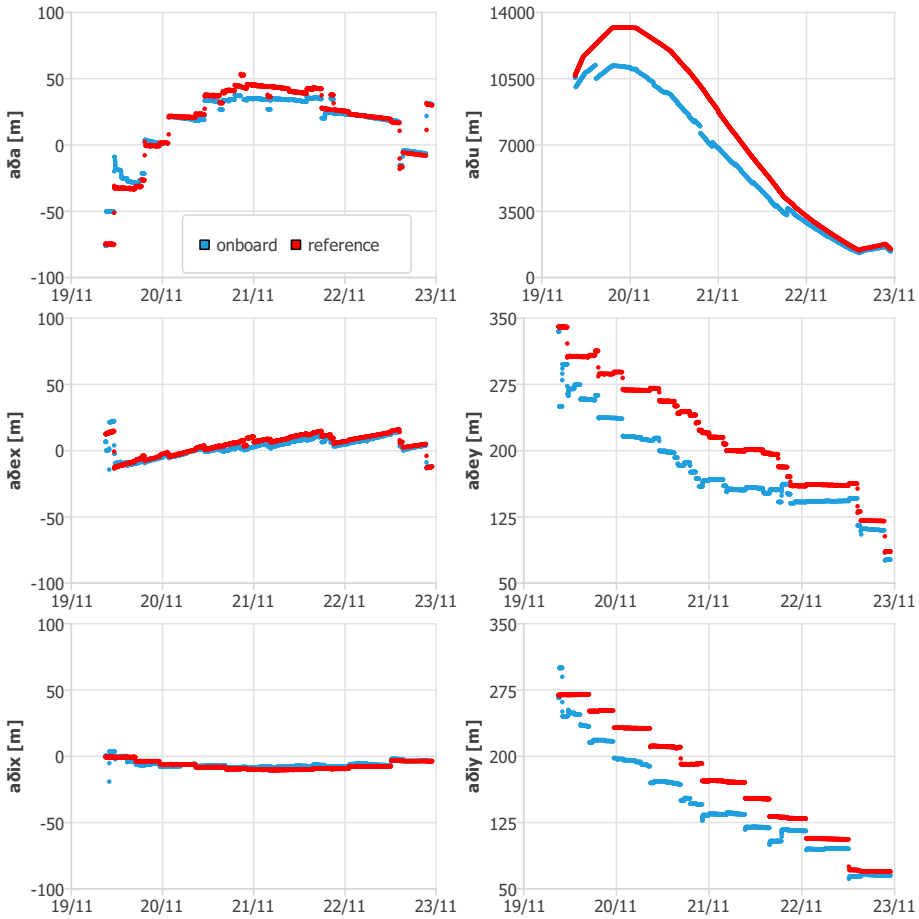

Figure 14: Onboard navigation solution (blue) vs. reference (red)

The filter was initialized with an a priori state $\boldsymbol{x}_0$ with the following components: δa=-50 m, $\delta \boldsymbol{e}$=(0 250) m, $\delta \boldsymbol{i}$=(0 300) m, δu=10000 m and $\delta \dot{a}$=0 m/s at epoch t_0=2016/11/19 9:00 UTC. According to Figure 14, this corresponds to an initial state error of a few dozen meters. As already mentioned in Section 3.5, this does not really reflect the uncertainties of the TLEs. This choice has been motivated by the preliminary analyses of the commissioning phase, which showed that large initialization errors could cause a filter divergence in case of sparse measurements. As a result, the support of a more robust on-ground vision-based batch least-square filter had been requested to initialize the filter

with a more accurate value. Note that this additional aid does not really reduce the value of onboard autonomy, since this preliminary activity could be done for example as part of the coarse orbit phasing.

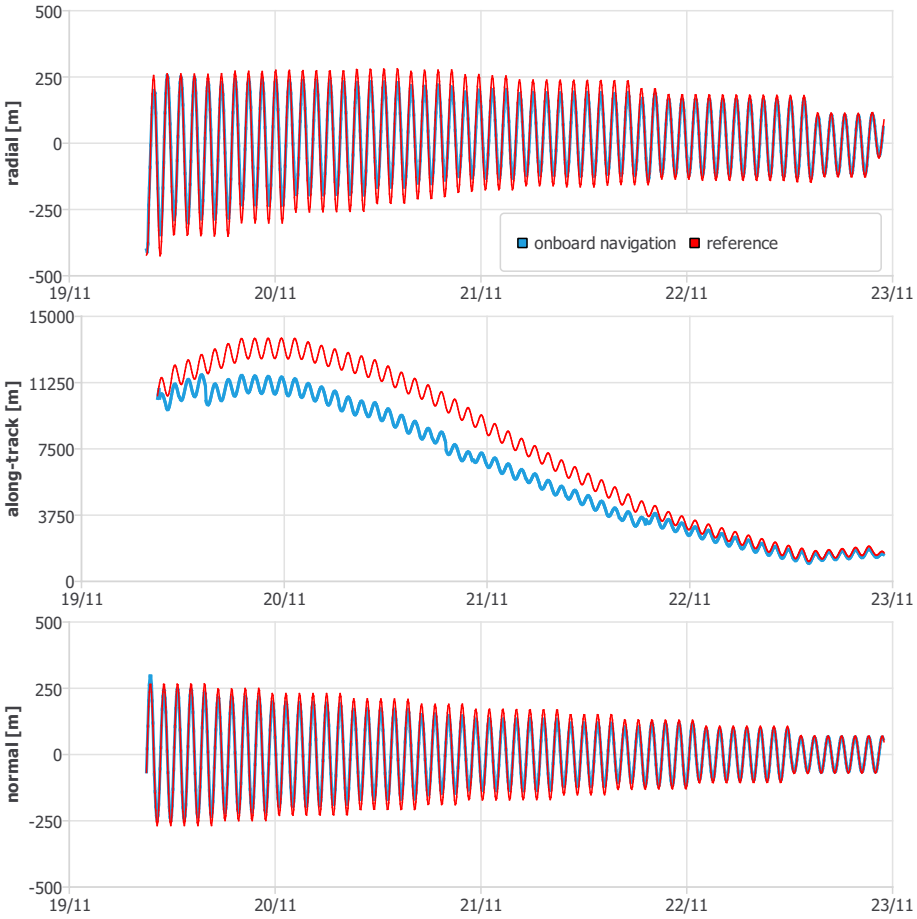

Figure 15: Onboard navigation solution (blue) vs. reference (red) mapped in the Cartesian frame $\mathcal{F}$

Overall, despite the sparse measurements, the filter convergence was achieved after a few orbits as depicted in Figure 14. For completeness, the relative motion is also depicted in the Cartesian local orbital frame $\mathcal{F}$ in Figure 15. The reference solution (in red in Figures 14 and 15) is the solution coming from the relative orbit determination done *a posteriori* on ground. Due to

the anisotropy of the problem, the resulting accuracy differs greatly among the orbital elements, especially for $a\delta u$ whose error amounts to several hundred meters at 10 km distance and diminishes to a few dozen meters at the end of the approach. The lateral accuracy is instead much better: $a\delta a$ is accurate to the meter level (ensuring thus a smooth approach) while the relative eccentricity and inclination vectors are accurately known a few orbits after the start of the approach to about 10% of their size. The beauty of this concept lies in the fact that the shape of the apparent motion can be estimated accurately in the early stage of the rendezvous allowing the establishment of a safe spiraling approach based on the proper phasing of $\delta \boldsymbol{e}$ and $\delta \boldsymbol{i}$.

The navigation errors can be better investigated in Fig. 16, which depicts the difference between the onboard navigation and the reference solution. The 3σ envelop derived from the covariance matrix is represented in gray in the background. The improvement of observability due to the execution of maneuvers can be observed by sudden reductions of errors. Despite the good convergence of the navigation solution, the covariance matrix is not representative of the navigation errors, denoting an improper filter tuning. As already mentioned in Section 3.5, further investigations are obviously needed to improve the filter behavior. This will be part of future work.

The difficulty of the filter's task given the poor visibility and presence of significant errors in the dynamical model should again be emphasized. Figure 17 summarizes the main sources of errors. Figure 17(a) depicts the maneuver execution errors (assessed post-facto on-ground using precise GPS-based orbit determination). It can be observed that undesired maneuver errors up to 6 mm/s were encountered during the experiment, which is a large value while dealing with precise formation-flying (the typical maneuver size during the approach amounts to 1-2 cm). In fact, the maneuver errors might still be acceptable from a guidance and control point of view but are a real issue for the navigation, since the improvement of the observability relies on well-known maneuvers. Figure 17(b) focuses instead on the unmodeled differential drag due to the variations of the cross-sectional area. This area has been reconstituted post-facto using

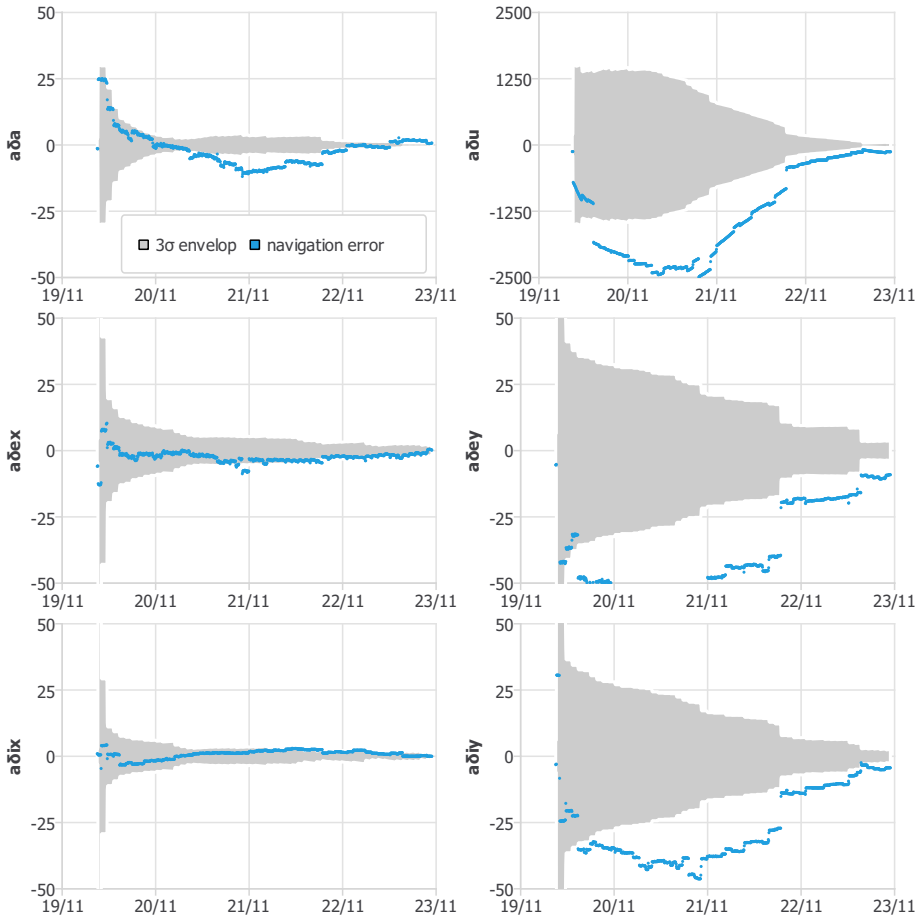

Figure 16: Navigation errors.

attitude data and is associated with the left axis of the plot. Note how this value can vary as much as 100% during the cool-down phases corresponding to the noticeable blue peaks (cf. Figure 3(c)). The cross-sectional area interacts with the atmosphere density, which varies substantially along the orbit (day-night variations), to create a differential drag force. The mean value (over one orbit) of the differential drag force - computed also post facto using a simple Harris-Priester model and assuming an identical drag coefficient for both spacecraft - is plotted in green (associated to the right axis of Figure 17(b)). In principle, the attitude of the target spacecraft also impacts the differential drag. This attitude

is unknown, because the target is noncooperative. However, in the particular case of the AVANTI experiment, the variations of the cross-section of the target can be neglected in view of the symmetry of picosatellite.

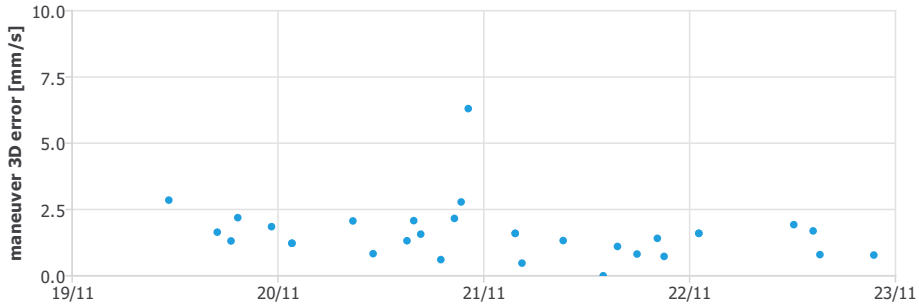

(a) Maneuver errors

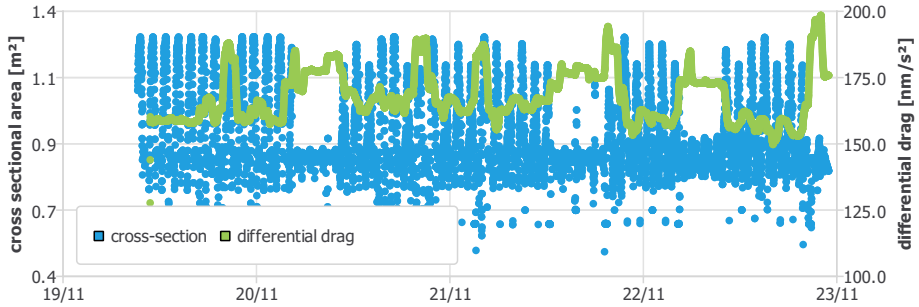

(b) Differential drag

Figure 17: Main errors of the onboard dynamical model

The filter is designed to estimate $a\delta\dot{a}$, that is, the mean effect of this differential drag on the relative semi-major axis. This value is depicted in Figure 18. Note that the decay of relative semi-major axis $a\delta\dot{a}$ can be mapped linearly into a differential drag ($a_d = na\delta\dot{a}/2$). Fig. 18 depicts both values using two different vertical axes. Given the small number of measurements and the weak observability, it seems that this task is too demanding for the filter. A quick look at Figures 17(b) and 18 indicates that the filter is not able to follow these unexpected rapid changes in differential drag, thus inducing errors in the dynamical model which have to be compensated with process noise. This constitutes an

important lesson learned for future similar applications. In order to improve the response of the filter, a better onboard modeling of the attitude-dependent differential drag might be necessary. This aspect will be investigated in a future work as part of the experiment post-analysis activities.

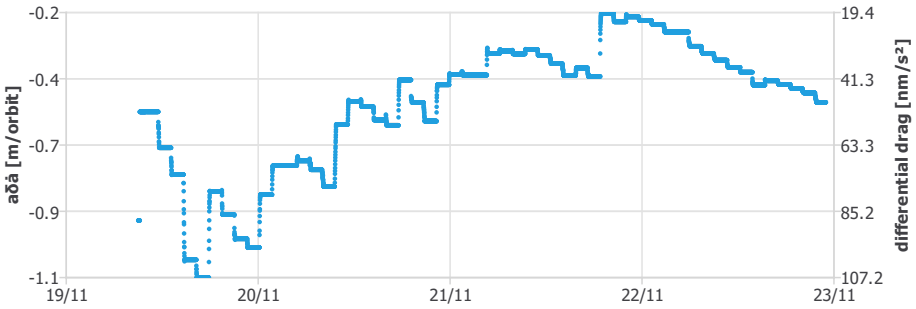

Figure 18: Estimated decay of relative semi-major axis. The right axis represents the equivalent differential drag necessary to produce such a decay.

4.2. Mid to Close Range Autonomous Approach

The second autonomous approach intended to investigate the main difficulties encountered when the separation decreases. At close-range, the navigation task becomes much more challenging due to the following reasons:

- When the distance decreases, the errors of the centroids (which should correspond to the center of mass) increase because the target is not imaged as a point anymore (as seen in Figure 19) so that the errors of the line-of-sight measurements are larger (as already observed in Figure 13).

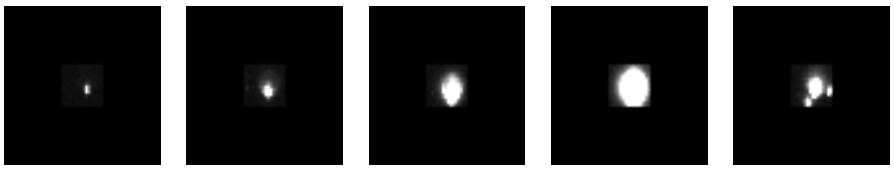

(a) 12 km (b) 5 km (c) 1 km (d) 540 m (e) 95 m

Figure 19: Target image at different distances

- At a certain point, the increasing brightness of the target object makes the use of an electronic shutter mandatory, in order to limit the exposure time. The collateral damage is that the stars are not visible anymore in the background, making a precise measurement of the orientation of the camera impossible. Thus the onboard filter has to rely on the onboard attitude estimation to determine the direction of the camera. In the case of AVANTI, the onboard attitude estimation could not always rely on star trackers, since one head was already blinded by the target object and the other could not always be oriented to deep sky. As a result, the onboard attitude error was sometimes affected by errors up to one degree (cf. Figure 20). This is another important lesson learned [1]: a similar mission dealing with close-proximity should ensure that at least one star tracker is always working, for example by using a third camera head (which was not available in AVANTI). However, it has to be kept in mind that one degree line-of-sight measurement error does not have the same impact at 100 m (1.7 m) as at 40 km (700 m). It is thus possible to cope with this error by tuning the filter measurement noise (cf. Table 2). In fact, during the close approach, this value was changed on 25 November 15:00 UTC from 80" (corresponding to 1 pixel) to 1000" in view of the poor onboard attitude estimation performance.

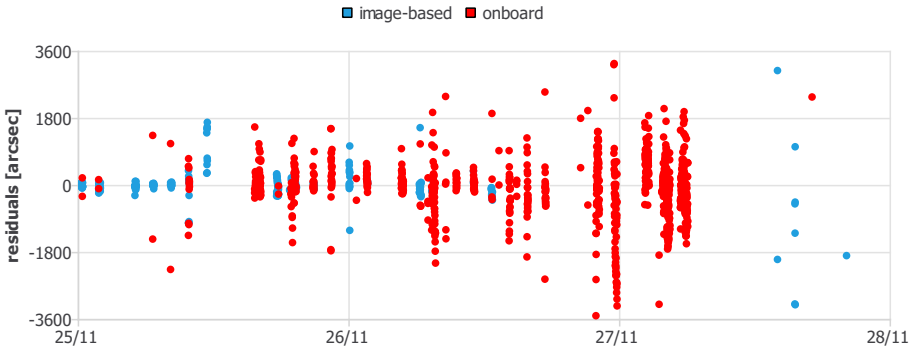

Figure 20: Filter residuals using image-based vs. onboard attitude estimation

- At close range, the cross-sectional area subject to the differential drag suffers from additional variations, in order to follow the target flying on a spiraling relative motion. This effect was limited from far to mid range. At large separations, the apparent relative motion is small so that it is enough to point the camera in the flight direction to observe it entirely. However, when the distance decreases, the camera might need to point in radial or cross-track directions to follow the target. As depicted in Figure 21, the differential drag becomes very different from the values observed previously (Figure 17(b)).

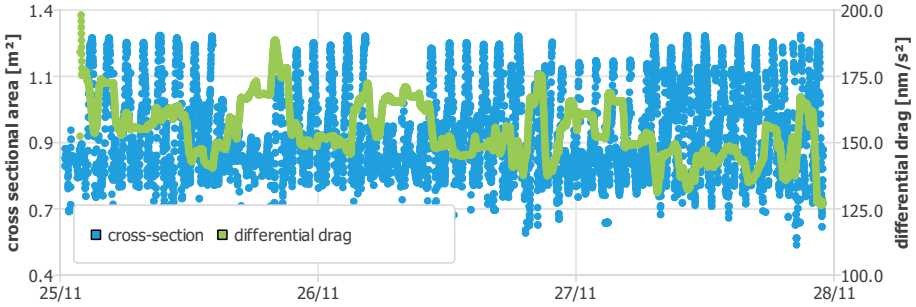

Figure 21: Cross-sectional area and differential drag at mid to close range

- Given the limited field of view of the camera (14°x 18°), a precise real-time knowledge of the relative motion is necessary to point the camera in the proper direction. In view of the aforementioned difficulties (inaccurate measurements and large perturbations of the onboard relative motion model), it becomes a real challenge to properly point the camera towards the target. Figure 22 depicts the real-time errors of the estimated direction to the target. From November 27^{th}, the errors become so large that the camera points in the wrong direction, making measurement updates impossible and eventually leading to a filter divergence. The fact that images are taken only every 30 seconds constitutes one of the major limitations of the navigation system. It would have probably been more robust (if the satellite would have allowed it) to work at a higher frequency (e.g. 1 Hz)

and to implement a simple attitude feedback controller to always keep the bright object in the center of the field of view so that the navigation filter would have always been fed with measurements.

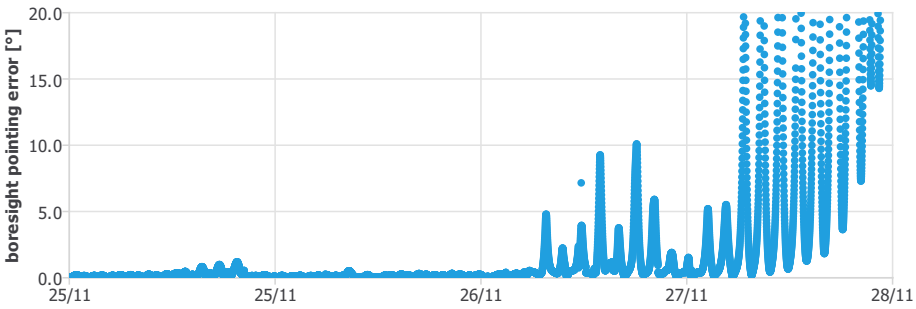

Figure 22: Onboard estimation errors of the direction to the target

Further investigations will be needed to investigate the stability of the filter. Early analyses tend to indicate that the filter is robust during the approaches, but becomes instable when the chaser reaches its final destination. This is probably due to the fact that the large maneuvers (a few cm/s) executed during the rendezvous are frequently contributing to improve the observability. At the end of the rendezvous, only small maneuvers (a few mm/s) are required to maintain the formation. The resulting improvement of observability is not enough to compensate the uncertainties brought by the unknown differential drag. The AVANTI experiment was fortunately designed to be robust against such issues. To that end, a finite-time horizon controller is implemented onboard to perform the approach [1]. In this control scheme, an open-loop guidance plan is generated and updated autonomously at a low frequency (maximum a few times per day). Consequently, the relative navigation is used only to update the plan or generate a new one but, during the execution of the plan, the guidance and control work in open-loop. Since the filter divergence happened at the end of the guidance plan, no maneuver was foreseen anymore by the controller. Thanks to the passive safety offered by the spiraling motion, no emergency action was required. After half a day, the strong differential drag made the target drift back to a few hundred meters separation. It was then sufficient to and point

the camera in the along-track direction to be able to see the target again and recover the formation.

Despite all these difficulties, the filter was able support the onboard guidance and control throughout the entire approach from 3 km to 50 m, and could deliver a reliable navigation solution during the approach. Fig. 23 depicts the achieved intersatellite separation and the time at which measurements were available (red dots). The blue dots correspond to the time of the four images. Note how

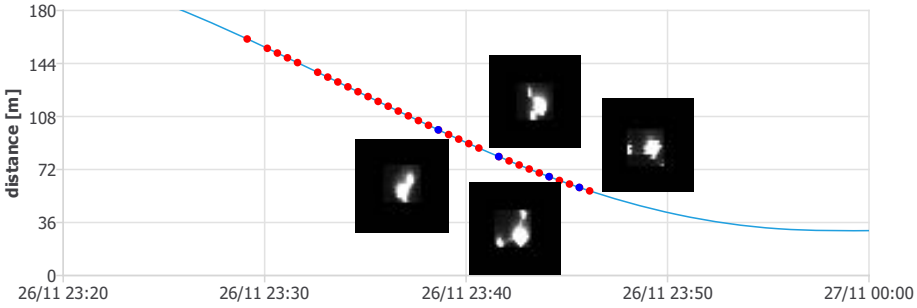

Figure 23: Measurements during the close range approach

the rectangular shape and the antennas of the spacecraft become visible when the distance decreases below 100 m. In a mission dedicated to close-proximity operations, this corresponds exactly to the range where other kinds of metrology can be used (pose estimation, stereo vision, radar,...).

5. Conclusion

The capability to autonomously approach a truly noncooperative object in orbit using a single camera has been demonstrated. This achievement was made possible thanks to the real-time angles-only relative navigation system embarked by the chaser satellite, which could successfully support the onboard guidance and control tasks to perform smooth and safe rendezvous.

Dealing with onboard autonomy, special attention has been paid to ensure the integrity of the real-time navigation solution, focusing in particular on the early stages of the process, that is, in the extraction of the line-of-sight measure-

ments. For this purpose, a novel approach has been employed to decouple as much as possible the target recognition task from the navigation filter. Based on the kinematic analysis of visible relative trajectories of non-stellar objects, the target detection algorithm is able to recognize the desired target object when initiating the approach at far-range using only coarse relative state information. After the convergence of the filter, the onboard navigation solution is used as backup in case of failed kinematic detection, together with additional detection capability based on the obvious brightness of the target object at close-range.

The line-of-sight measurements are subsequently processed by a dynamical filter. In order to cope with the limited onboard resources, an Extended Kalman Filter has been implemented, based on an analytical model of the relative motion which takes into account the perturbations due to the Earth oblateness and due to the differential drag. During the experiment, the filter had to face severe navigation conditions, characterized by a poor visibility and strong orbit perturbations. In fact only 10 minutes of observations could be collected every orbit. Furthermore, the onboard dynamical model was affected by strong unknown maneuver execution errors and unknown variations of differential drag.

Despite these difficulties, the relative navigation system was able to support two different autonomous approaches, first from 13 km to 1 km separation, then from 3 km to 50 m. At far-range, despite line-of-sight measurements accurate at the arcminute level, the poor observability is responsible for large longitudinal errors up to a few kilometers. This error decreases steadily during the rendezvous as the observability improves. A final longitudinal error of a few dozen meters is achieved when reaching the final destination at 1 km separation. At close-range, lateral navigation performance at the meter level is achieved during the rendezvous.. The unknown varying differential drag revealed itself however to be a source of troubles. Further investigations are needed to enhance the onboard modelling of the differential drag and to better tune the filter, in order to further improve the robustness of the navigation solution.

Overall, the experiment demonstrated the power of angles-only navigation. Despite its simplicity, a simple camera is able to support autonomous rendezvous

from several dozen kilometers to only 50 m, paving the way to future close-proximity operations.

6. Acknowledgments

The construction of the BIROS satellite was funded by the Federal Ministry of Education and Research of Germany (BMBF) (project number FKZ 01LK0904A).

References

[1] G. Gaias, J.-S. Ardaens, Flight Demonstration of Autonomous Noncooperative Rendezvous in Low Earth Orbit, Journal of Guidance, Control, and Dynamics,accessed, 16 Nov 2017.

[2] W. Halle, W. Bärwald, T. Terzibaschian, M. Schlicker, K. Westerdorf, The DLR -Satellite BIROS in the Fire-Bird Mission, in: Proceedings of the 4S Symposium: Small Satellites, Systems and Services, 26 - 30 May 2014, Majorca, Spain, European Space Agency, Noordwijk, The Netherlands, 2014.

[3] F. Baumann, S. Trowitzsch, K. Brieß, BEESAT - A CubeSat Series Demonstrates Novel Picosatellite Technologies, 4$^{\text{th}}$ European CubeSat Symposium, Brussels, Belgium, 2012.

[4] S. Roemer, S. Stoltz, SPL Light Weight Deployment Mechanism for Single CubeSats and DPL for Double CubeSats, Symposium on Small Satellite Systems and Services (4S), Funchal, Madeira, Portugal, 2010.

[5] S. D'Amico, J.-S. Ardaens, G. Gaias, H. Benninghoff, B. Schlepp, J. L. Jørgensen, Noncooperative Rendezvous Using Angles-Only Optical Navigation: System Design and Flight Results, Journal of Guidance, Control, and Dynamics 36 (6) (2013) 1576–1595, doi: 10.2514/1.59236.

[6] S. Weiß, F. Kempe, K. Brieß, GPS Tracking on the Three-Axis-Stabilized Picosatellite BEESAT-4, no. N.A., 7th Pico and Nano Satellite Workshop on Technology for Small Satellite Research, Würzburg, Germany, 2013.

[7] R. J. V. Chari, Autonomous Orbital Rendezvous Using Angles-Only Navigation, Ph.D. thesis, Massachusetts Institute of Technology. Dept. of Aeronautics and Astronautics., U.S.A (2001).

[8] D. C. Woffinden, Angles-Only Navigation for Autonomous Orbital Rendezvous, Ph.D. thesis, Utah State University, U.S.A (2008).

[9] S. C. Nardone, V. J. Aidala, Observability Criteria for Bearings-Only Target Motion Analysis, IEEE Transactions on Aerospace and Electronic Systems 17 (2) (1981) 162–166.

[10] S. E. Hammel, V. J. Aidala, Observability Requirements for Three-Dimensional Tracking via Angle Measurements, IEEE Transactions on Aerospace and Electronic Systems 21 (2) (1985) 200–207.

[11] D. C. Woffinden, D. K. Geller, Observability Criteria for Angles-Only Navigation, IEEE Transactions on Aerospace and Electronic Systems 45 (3) (2009) 1194–1208.

[12] J. R. Yim, J. L. Crassidis, J. L. Junkins, Autonomous Orbit Navigation of Two Spacecraft System Using Relative Line of Sight Vector Measurements, no. 04-257, 14th AAS/AIAA Space Flight Mechanics Meeting, Maui, Hawaii, 2004.

[13] J. Grzymisch, W. Fichter, Optimal Rendezvous Guidance with Enhanced Bearings-Only Observability, Journal of Guidance, Control, and Dynamics 38 (6) (2015) 1131–1140, doi: 10.2514/1.G000822.

[14] F. Sullivan, S. D'Amico, Adaptive Filtering for Maneuver-Free Angles-Only Navigation in Eccentric Orbits, 27th AAS/AIAA Space Flight Mechanics Meeting, San Antonio, Texas, 2017.

[15] DARPA archive: Orbital express on-orbit mission updates, `http://archive.darpa.mil/orbitalexpress/mission_updates.html`, DARPA Tactical Technology Office, [retrieved 4 August 2017] (Jul. 2007).

[16] S. Persson, B. Jakobsson, E. Gill, PRISMA - Demonstration Mission for Advanced Rendezvous and Formation Flying Technologies and Sensors, no. 05-B56B07, 56$^{\text{th}}$ International Astronautical Congress, Fukuoka, Japan, 2005.

[17] R. Noteborn, P. Bodin, R. Larsson, C. Chasset, Flight Results from the PRISMA Optical Line of Sight Based Autonomous Rendezvous Experiment, in: Proceedings of the 4$^{\text{th}}$ International Conference on Spacecraft Formation Flying Missions & Technologies (SFFMT), Canadian Space Agency, St-Hubert, Quebec, 2011.

[18] M. Delpech, J.-C. Berges, S. Djalal, J. Christy, Vision Based Rendezvous Experiment performed during the PRISMA Extended Mission, in: Proceedings of the 23$^{\text{rd}}$ International Symposium on Space Flight Dynamics, Jet Propulsion Laboratory, Pasadena, California, USA, 2012.

[19] M. Benn, J. L. Jrgensen, Autonomous Vision Based Detection of Non-stellar Objects Flying in Formation with Camera Point of View, in: Proceedings of the 5$^{\text{th}}$ International Conference on Spacecraft Formation Flying Missions & Technologies (SFFMT), DLR, German Space Operations Center, Munich, Germany, 2013.

[20] H. Benninghoff, T. Tzschichholz, T. Boge, G. Gaias, A Far Range Image Processing Method for Autonomous Tracking of an Uncooperative Target, 12$^{\text{th}}$ Symposium on Advanced Space Technologies in Robotics and Automation, Noordwjik, The Netherlands, 2013.

[21] J.-S. Ardaens, G. Gaias, Angles-Only Relative Orbit Determination in Low Earth Orbit, submitted to Advances in Space Research, under review.

[22] P. B. Davenport, A Vector Approach to the Algebra of Rotations with Applications, NASA x-546-65-437, NASA (Nov. 1965).

[23] M. Ester, H.-P. Kriegel, J. Sander, X. Xu, A Density-Based Algorithm for Discovering Clusters in Large Spatial Databases with Noise, in: Proceedings of the 2nd International Conference on Knowledge Discovery and Data mining, 1996, p. 226231.

[24] G. Gaias, S. D'Amico, J.-S. Ardaens, Angles-Only Navigation to a Noncooperative Satellite Using Relative Orbital Elements, Journal of Guidance, Control, and Dynamics 37 (2) (2014) 439–451, doi: 10.2514/1.61494.

[25] O. Montenbruck, M. Kirschner, S. D'Amico, S. Bettadpur, E/I-Vector Separation for Safe Switching of the GRACE Formation, Aerospace Science and Technology 10 (7) (2006) 628–635, doi: 10.1016/j.ast.2006.04.001.

[26] J.-S. Ardaens, S. D'Amico, Spaceborne Autonomous Relative Control System for Dual Satellite Formations, Journal of Guidance, Control, and Dynamics 32 (6) (2009) 1859–1870.

[27] S. D'Amico, J.-S. Ardaens, R. Larsson, Spaceborne Autonomous Formation-Flying Experiment on the PRISMA Mission, Journal of Guidance, Control, and Dynamics 35 (3) (2012) 834–850, doi: 10.2514/1.55638.

[28] G. Gaias, J.-S. Ardaens, O. Montenbruck, Model of J2 Perturbed Satellite Relative Motion with Time-Varying Differential Drag, Celestial Mechanics and Dynamical Astronomy 123 (4) (2015) 411–433, doi: 10.1007/s10569-015-9643-2.

[29] J.-Y. Bouguet, Camera Calibration Toolbox for Matlab, `http://www.vision.caltech.edu/bouguetj/calib_doc/` [Accessed 1 September 2017] (2004).

[30] R. Kahle, M. Weigel, M. Kirschner, S. Spiridonova, E. Kahr, K. Letsch, Relative Navigation to Non-cooperative Targets in LEO: Achievable Accuracy

from Radar Tracking Measurements, Int. J. Space Science and Engineering 2 (1) (2014) 81–95.